Spectral element/smoothed profile method for turbulent flow simulations of waterjet propulsion systems

Spectral Element/Smoothed Profile Method for Turbulent Flow Simulations of Waterjet Propulsion Systems

Xian Luo*, Chryssostomos Chryssostomidis* and George Em Karniadakis**
*** Design Laboratory, MIT Sea Grant, MIT ** Division of Applied Mathematics, Brown University**

Keywords: ship propulsion, CFD, high-order methods, immersive boundary method

Abstract

We have developed fast numerical algorithms [1] for flows with complex moving domains, e.g. propellers in free-space and impellers in waterjets, by combining the smoothed profile method (SPM, [2, 3, 4]) with the spectral element method [5]. The new approach exhibits high-order accuracy with respect to both temporal and spatial discretizations. Most importantly, the method yields great computational efficiency as it uses fixed simple Cartesian grids and hence it avoids body-conforming mesh and remeshing. To simulate high Reynolds number flows, we incorporate the Spalart-Allmaras turbulence model and solve the unsteady Reynolds-averaged Navier-Stokes (URANS) equations. We present verification of the method by studying the turbulent boundary layer over a flat plate. We show that both the eddy viscosity and velocity fields are resolved very accurately within the boundary layer. Having developed and validated our numerical approach, we apply it to study transitional and turbulent flows in an axial-flow waterjet propulsion system. The efficiency and robustness of our method enable parametric study of many cases which is required in design phase. We present performance analysis and show the agreement with experimental data for waterjets.

1. INTRODUCTION

Design optimization of waterjet using computational fluid dynamics (CFD) tools will lead to more efficient designs that are smaller and may alleviate cavitation problems. However, for problems with such complex moving 3D geometries as rotors and stators in waterjets, standard CFD tools are inefficient due to the very large computational time and the complex meshes required. For many simulations of waterjets, potential flows are assumed with limited viscous corrections, e.g. based on a two dimensional integral boundary layer analysis [6]. There have been some RANS solvers applied to waterjet simulations, but numerical simulations of the interaction between rotor and stator in a fully unsteady manner are too complicated and computationally expensive. So many assumptions have been made, e.g. the rotor and stator problem is decoupled and the flow is rotationally cyclic so that one can model a single blade passage only [7].

To this end, we aim to develop fast high-order algorithms for numerical simulations of flows with complex moving domains, based on fixed simple Cartesian grids. In this paper we first review our numerical approach ([8]) where we combine the smoothed profile method (SPM, [2, 3, 4]) with the spectral element method [5]. SPM is similar to the immersed boundary method (IBM, [9]) as they both use a force distribution to effectively approximate the boundary conditions and hence to impose the rigid-body constraints. However, with the spectral element discretization SPM leads to high-order accuracy as SPM adopts a smooth indicator function in contrast to the direct delta function used in IBM. Furthermore, the hybrid methodology leads to high computational efficiency; it is much faster (typically 1000 times faster) than using the often-employed arbitrary Lagrangian Eulerian (ALE) for simulations in moving complex domains.

Waterjet pumps often operate in high Reynolds number regime and the flow is turbulent, so we incorporate the Spalart-Allmaras (SA) turbulence model and solve the URANS equations to account for the subgrid stresses. We show that the method resolves accurately the turbulent boundary layer over a flat plate at Reynolds number $Re = 10^7$. Subsequently, we present full 3D flow simulations of a waterjet propulsion system and perform a parametric study.

2. NUMERICAL METHODOLOGY

2.1. Representation of moving bodies

SPM represents the moving bodies by smoothed profiles (or the so-called indicator functions), which equal *unity* inside the moving domains, *zero* in the fluid domain, and vary smoothly between one and zero in the solid-fluid interfacial domain. In [1] we proposed a *general* form, which is effective for *any* domain shape such as a propeller, i.e.,

$$\phi_i(\mathbf{x},t) = \frac{1}{2}\left[\tanh\left(\frac{-d_i(\mathbf{x},t)}{\xi_i}\right)+1\right], \qquad (1)$$

where index i refers to the i_{th} moving body (e.g., a single blade of rotor or stator). Also, ξ_i is the interface thickness parameter and $d_i(\mathbf{x},t)$ is the *signed* distance to the i_{th} moving body with positive value outside and negative inside. For simple geometries (cylinders, ellipsoids, etc.) $d_i(\mathbf{x},t)$ can be obtained analytically. However, for general complex shapes, such as impellers which can be represented by many surface point coordinates, spline interpolations are used to cal-

culate $d_i(\mathbf{x},t)$ and thus $\phi_i(\mathbf{x},t)$. A smoothly spreading indicator function is achieved by summing up the indicator functions of all the N_p non-overlapping moving bodies: $\phi(\mathbf{x},t) = \sum_{i=1}^{N_p} \phi_i(\mathbf{x},t)$.

Based on this indicator function, the *velocity field* of the moving bodies, $\mathbf{u}_p(\mathbf{x},t)$, is constructed from the rigid-body motions of each moving domain:

$$\phi(\mathbf{x},t)\mathbf{u}_p(\mathbf{x},t) = \sum_{i=1}^{N_p} \{\mathbf{V}_i(t) + \omega_i(t) \times [\mathbf{x} - \mathbf{R}_i(t)]\} \phi_i(\mathbf{x},t), \tag{2}$$

where $\mathbf{R}_i$, $\mathbf{V}_i = \frac{d\mathbf{R}_i}{dt}$ and ω_i are spatial positions, translational velocity and angular velocity of the i_{th} moving body, respectively. The *total velocity field* is then defined by a smooth combination of both the velocity field of moving bodies $\mathbf{u}_p$ and the fluid velocity field $\mathbf{u}_f$:

$$\mathbf{u}(\mathbf{x},t) = \phi(\mathbf{x},t)\mathbf{u}_p(\mathbf{x},t) + (1-\phi(\mathbf{x},t))\mathbf{u}_f(\mathbf{x},t). \tag{3}$$

We see that inside the moving domains ($\phi = 1$), we have $\mathbf{u} = \mathbf{u}_p$, i.e., the total velocity equals the velocity of the moving body. At the interfaces ($0 < \phi < 1$), the total velocity changes smoothly from the propeller velocity $\mathbf{u}_p$ to the fluid velocity $\mathbf{u}_f$.

SPM imposes the no-penetration constraint on the surfaces of the simulated moving bodies. It can be shown (ref. [1]) that imposing the incompressibility condition of the total velocity $\nabla \cdot \mathbf{u} = 0$ ensures the no-penetration surface condition $(\nabla\phi) \cdot (\mathbf{u}_p - \mathbf{u}_f) = 0$, and vice versa.

SPM solves for the total velocity, $\mathbf{u}$, in the entire domain D, including inside the moving domains, using the incompressible Navier-Stokes equations with an extra force density term, i.e.,

$$\frac{\partial \mathbf{u}}{\partial t} + (\mathbf{u}\cdot\nabla)\mathbf{u} = -\frac{1}{\rho}\nabla p + \nu\nabla^2\mathbf{u} + \mathbf{f}_s \quad \text{in } D \tag{4a}$$

$$\nabla \cdot \mathbf{u} = 0 \quad \text{in } D, \tag{4b}$$

where ρ is the density of the fluid, p is the pressure field, ν is the kinematic viscosity of the fluid, $\mathbf{g}$ is the gravity (and other external forces on the fluid), and the fluid solvent is assumed to be Newtonian with constant viscosity for simplicity.

Here $\mathbf{f}_s$ is the body force density term representing the interactions between the moving bodies and the fluid. SPM assigns $\int_{\Delta t} \mathbf{f}_s dt = \phi(\mathbf{u}_p - u)$ to denote the momentum change (per unit mass) due to the presence of the moving bodies. Thus, at each time step the flow is corrected by a momentum impulse to ensure that the total velocity matches that of the rigid domains within the moving domain, hence enforcing the rigidity constraint.

2.2. Fully-discrete system: temporal and spatial discretizations

To numerically solve equations (4), we developed a high-order temporal discretization [1] instead of the original fully-explicit scheme ([2]). We introduced a semi-implicit treatment, using a stiffly-stable high-order *splitting* (velocity-correction) scheme [10]. In particular, the viscous term is treated implicitly and the order of the time integration scheme is up to 3rd. This choice enhances the stability and also increases the temporal accuracy of the original SPM implementation.

The hydrodynamic force $\mathbf{F}_h$ and torque $\mathbf{Q}_h$ on the moving bodies exerted by the surrounding fluid are derived from the momentum conservation. Specifically, the momentum change in the moving domains equals the time integral of the hydrodynamic force and the external force, and hence:

$$\mathbf{F}_{h_i}^{\,n} = \frac{1}{\Delta t}\int_D \rho\phi_i^{n+1}(\mathbf{u}^* - \mathbf{u}_p^n)d\mathbf{x} \tag{5a}$$

$$\mathbf{Q}_{h_i}^{\,n} = \frac{1}{\Delta t}\int_D \mathbf{r}_i^{n+1} \times [\rho\phi_i^{n+1}(\mathbf{u}^* - \mathbf{u}_p^n)]d\mathbf{x} \tag{5b}$$

where the indices $n, n+1$ refer to the solutions at different time steps, $\mathbf{u}^*$ is the intermediate velocity field in the splitting scheme, and $\mathbf{r}_i^{n+1}$ is the distance vector from the rotational reference point on the i_{th} moving body to any spatial point $\mathbf{x}$.

For spatial discretization, we apply the spectral/hp element method (see [5]). This hybrid method benefits from both finite element and spectral methods: on one hand, for domains with complex geometry, we can increase the number of subdomains/elements (h-refinement) with the error in the numerical solution decaying algebraically. On the other hand, with fixed elemental size we can increase the interpolation order within the elements (p-refinement) to achieve an exponentially decaying error, provided the solutions are sufficiently smooth throughout the domain. The spectral element method has great advantages because of its dual path to convergence, e.g. convergence check without re-meshing. Furthermore, the use of smooth profiles in SPM preserves the high-order numerical accuracy of the spectral element method.

The spectral/hp element method allows us to accurately represent arbitrary fixed rigid boundaries of the flow domain while using SPM allows us to represent the moving/complex domains, e.g. impellers and stators.

2.3. Turbulence modeling

The Spalart-Allmaras (SA) model [11] is a one-equation model, which solves a transport equation for a viscosity-like variable $\tilde{\nu}$, which may be referred to as the SA variable, i.e.,

$$\frac{\partial\tilde{\nu}}{\partial t} + \mathbf{u}\cdot\nabla\tilde{\nu} = C_{b1}[1-f_{t2}]\tilde{S}\tilde{\nu} - \left[C_{w1}f_w - \frac{C_{b1}}{\kappa^2}f_{t2}\right]\left(\frac{\tilde{\nu}}{d}\right)^2 + \frac{1}{\sigma}\{\nabla\cdot[(\nu+\tilde{\nu})\nabla\tilde{\nu}] + C_{b2}|\nabla\tilde{\nu}|^2\} + f_{t1}\Delta U^2 \tag{6}$$

where the RHS consists of the production, destruction, diffusion and trip terms respectively. Here the modified mean strain rate $\tilde{S} \equiv S + \frac{\tilde{\nu}}{\kappa^2 d^2} f_{v2}$, where $f_{v2} = 1 - \frac{\chi}{1+\chi f_{v1}}$, $S_{ij} = \sqrt{2\Omega_{ij}\Omega_{ij}}$, and $\Omega_{ij} = \frac{1}{2}(\frac{\partial u_i}{\partial x_j} - \frac{\partial u_j}{\partial x_i})$. Moreover, the wall function is $f_w = g\left[\frac{1+C_{w3}^6}{g^6+C_{w3}^6}\right]^{1/6}$, $g = r + C_{w2}(r^6 - r)$, $r = \frac{\tilde{\nu}}{\tilde{S}\kappa^2 d^2}$, where d is the distance to the closest surface and the constants (e.g. C_{b1}, C_{b2}) follow the definitions in [11].

We ignore the trip term (last term on RHS, $f_{t1} = 0$) and also $f_{t2} = 0$ for the simulations presented in this paper. According to studies of [12, 13], this simplification as opposed to the standard version probably makes very little difference, provided the proper boundary conditions are used. In our own tests, we found that the trip term f_{t1} (and $f_{t2} \neq 0$) helps to stabilize the flow for higher Reynoldes number (e.g. $Re > 200,000$).

The scalar equation (6) is discretized and solved in a similar manner as the Navier Stokes equations [1], i.e.,

$$\frac{\tilde{\nu}^s - \sum_{q=0}^{J_e-1} \alpha_q \tilde{\nu}^{n-q}}{\Delta t} = \sum_{q=0}^{J_e-1} \beta_q [-(\mathbf{u}^{n-q}\cdot\nabla)\tilde{\nu}^{n-q} +$$

$$C_{b1}\tilde{S}^{n-q}\tilde{\nu}^{n-q} - C_{w1} f_w{}^{n-q}\left(\frac{\tilde{\nu}^{n-q}}{d^{n-q}}\right)^2 + \frac{C_{b2}}{\sigma}|\nabla\tilde{\nu}^{n-q}|^2] \quad (7a)$$

$$\frac{\gamma_0\tilde{\nu}^* - \tilde{\nu}^s}{\Delta t} = \frac{1}{\sigma}\nabla\cdot[(\nu + \tilde{\nu}^n)\nabla\tilde{\nu}^*] \quad (7b)$$

$$\frac{\gamma_0\tilde{\nu}^{n+1} - \gamma_0\tilde{\nu}^*}{\Delta t} = \frac{\gamma_0\phi^{n+1}(\tilde{\nu}_p^{n+1} - \tilde{\nu}^*)}{\Delta t} \quad (7c)$$

where α_q, β_q and $\gamma_0 = \sum_{q=0}^{Je-1}\alpha_q$ are the scaled coefficients of the stiffly-stable scheme. In particular, the diffusion term is integrated semi-implicitly and the last substep (7c) is the SPM correction due to the moving bodies. Here $\tilde{\nu}_p^{n+1}$ is the SA viscosity field, which is defined everywhere including the moving domains: $\phi(\mathbf{x},t)\tilde{\nu}_p(\mathbf{x},t) = \sum_{i=1}^{N_p}\phi_i(\mathbf{x},t)\tilde{\nu}_i(t)$. The unsteady Reynolds-averaged Navier-Stokes (URANS) equations are solved with the eddy viscosity to account for the sub-grid stresses:

$$\frac{\partial\mathbf{u}}{\partial t} + (\mathbf{u}\cdot\nabla)\mathbf{u} = -\frac{1}{\rho}\nabla p + \nabla[(\nu+\nu_t)\nabla\mathbf{u}] + \mathbf{f}_s \quad (8a)$$

$$\nabla\cdot\mathbf{u} = 0 \quad \text{in } D. \quad (8b)$$

Here the Reynolds stress tensor is modeled by the Boussinesq assumption [14]: $-\overline{u'_i u'_j} = \nu_t\left(\frac{\partial u_i}{\partial x_j} + \frac{\partial u_j}{\partial x_i}\right)$, where ν_t is the turbulent eddy viscosity $\nu_t = \tilde{\nu} f_{v1}$, $f_{v1} = \frac{\chi^3}{\chi^3 + C_{v1}^3}$, $\chi = \frac{\tilde{\nu}}{\nu}$.

3. VERIFICATION: TURBULENT BOUNDARY LAYER OVER A FLAT PLATE

We applied the SPM-URANS approach to the benchmark problem of turbulent boundary layer over a flat plate. We compare our simulation results against the exact solution for SA viscosity (scaled by the kinematic viscosity, i.e. $\chi = \frac{\tilde{\nu}}{\nu}$) and against the Spalding velocity profile, which is an analytic fit to experimental data. We non-dimensionalize the length and velocity as $y^+ = \frac{yu_\tau}{\nu}$ and $u^+ = \frac{u}{u_\tau}$ where u_τ is the friction velocity $\sqrt{\frac{0.0135}{Re^{1/7}}}$.

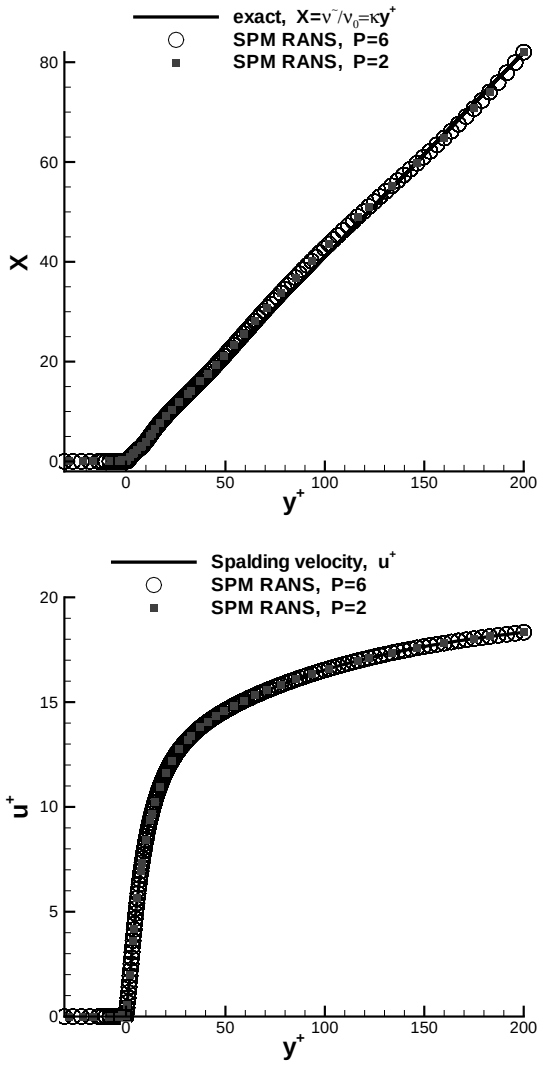

Figure 1. *Turbulent boundary layer over a flat plate*: SPM results compared against exact solutions for SA viscosity (upper) and velocity (lower), with two different polynomial orders for spectral element discretization $P = 2$ or $P = 6$.

Here the simulation domain is $[0,200]\times[-50,200]\times[0,20]$ (in viscous units), with the wall aligned with $y^+ = 0$ plane. For boundary conditions, we impose the exact solutions for viscosity and velocity at the inlet $x^+ = 0$, far-field

$y^+ = 200$ and in the wall $y^+ = -50$; periodicity is imposed in z-direction. In the spectral element discretization 440 hexahedral elements are used (22 elements in inter-wall direction) with polynomial order $P = 2 \sim 6$. Here the Reynolds number is $Re = 10^7$.

Figure 1 shows good agreement between SPM-RANS results and the validated solutions of SA viscosity and velocities. It also shows that by increasing the polynomial order from $P = 2$ and $P = 6$ there is no visible difference and it indicates that we have achieved convergence.

4. SIMULATIONS: WATERJET PROPULSION SYSTEMS

Having developed and validated our numerical approach, we apply it to study transitional and turbulent flows in an axial-flow waterjet propulsion system (AxWJ-1). Figure 2 shows the geometric configuration and numerical set-up for the simulations. While the simple boundaries (shaft, hub and casing) are treated in the standard way (i.e., applying directly Dirichlet boundary conditions), the rotor and stator blades are modeled with the smoothed profiles (equation (1)) to avoid body-conforming meshes. We set the rotor to have rotational speed ω and translational velocity $\mathbf{V} = \mathbf{0}$ in (2), which means the reference frame moves at the waterjet advance velocity V_a. We calculate the Reynolds number $Re = \frac{UD}{\nu} = \frac{nD^2}{2\nu}$ and the advance ratio $J = \frac{V_a}{nD}$, where the diameter of inlet $D = 12$ inch and $n = \omega/2\pi$. The non-dimensionalization factors for length and velocity are: 0.0254 *meter* (1 inch) and nD m/s.

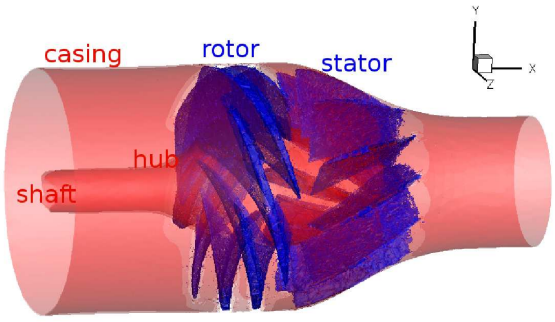

Figure 2. *Waterjet AxWJ-1*: Geometry description and numerical set-up with SPM modeling of rotor and stator.

We use a computational grid with 209,661 tetrahedral elements and polynomial order of 3 for the spectral element discretization. The boundary conditions include an upstream prescribed velocity inlet ($x = -6$ inch), which is non-uniform

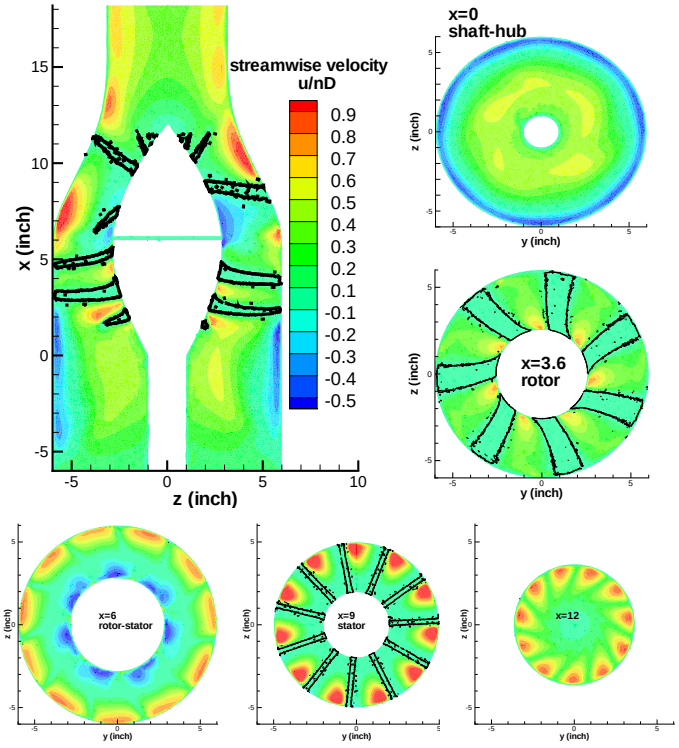

Figure 3. *SPM simulations of waterjet AxWJ-1 at* $Re = 57,906$ *and* $J = 0.1667$: Instantaneous streamwise velocity contour at different locations with the black lines showing the virtual boundaries of rotor and stator.

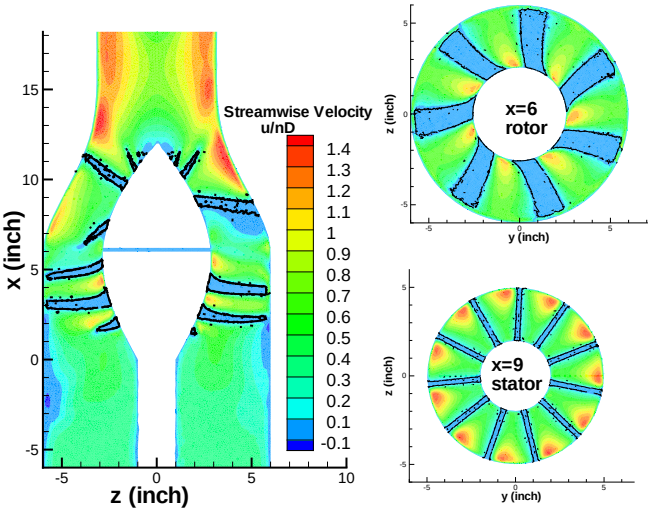

Figure 4. *SPM simulations of waterjet AxWJ-1 at* $Re = 57,906, J = 0.3333$: Instantaneous streamwise velocity contour in different locations.

near the walls to account for the boundary layer. The SA viscosity is given as $\tilde{\nu} = 3\nu$ at the inlet as suggested in [13, 15]. The downstream outlet ($x = 18$) is set to have a fixed pressure and zero Neumann condition for velocities. For initial conditions, we use zero velocity field and unit SA viscosity $\tilde{\nu} = \nu$ if not otherwise indicated.

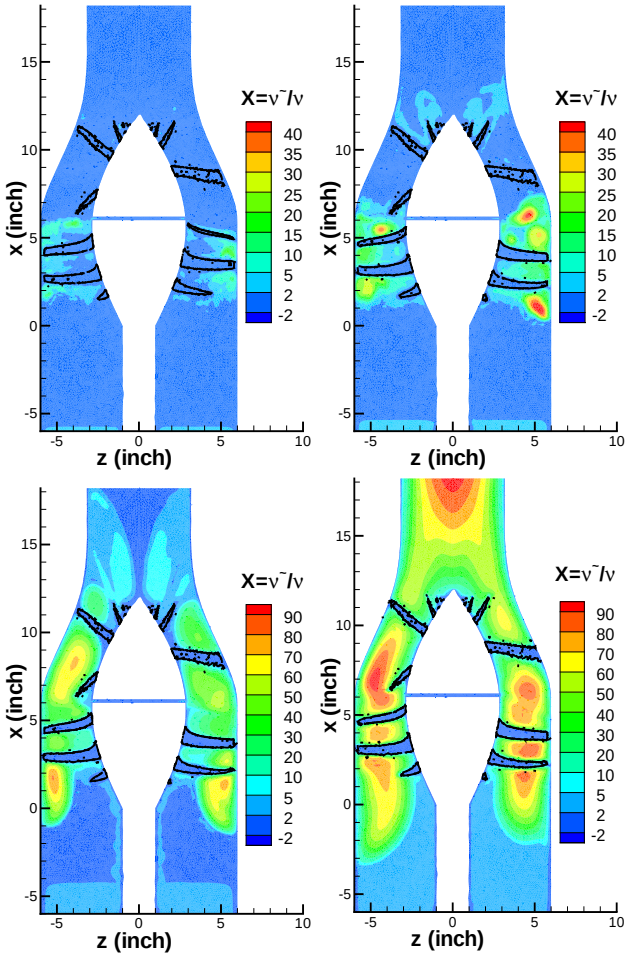

Figure 5. *SPM simulations of waterjet AxWJ-1 at* $Re = 57,906, J = 0.3333$: Contours of SA viscosity ($\chi = \frac{\tilde{\nu}}{\nu}$) at y=0 plane at 120, 840, 3000, 20000 steps ($\sim$ 5 evolutions).

First, we examine instantaneous flow fields inside the waterjet at $Re = 57,906$ with $J = 0.1667$. Figure 3 presents instantaneous streamwise velocity contours at different locations after 5 evolutions of the rotor in the simulation. The velocity is non-dimensionalized as $\frac{u}{nD}$, and the black lines indicate the boundaries of the rotor and stator blades ($\phi = 0.5$). The plot shows that the flow accelerates through the rotor and it is guided through the stator vanes to exit the nozzle as a jet. We also notice that there exist large pockets of *reversal flow* upstream of the rotor and also between the rotor and stator. In contrast, for a larger advance ratio $J = 0.3333$ as shown in figure 4, there is no significant reversal flow. Thus, our numerical approach is effective in identifying important flow features inside waterjet systems.

Figure 5 shows contours of SA viscosity ($\chi = \frac{\tilde{\nu}}{\nu}$) at y=0 plane at different time instances, where the last frame corresponds to 20000 time steps which is about 5 evolutions. We see that large SA viscosity is generated in the rotor region; it grows in time and propagates downstream through the stator. The plots also show that our numerical approach successfully captures the transition from the laminar flow near the inlet to the turbulent flow downstream.

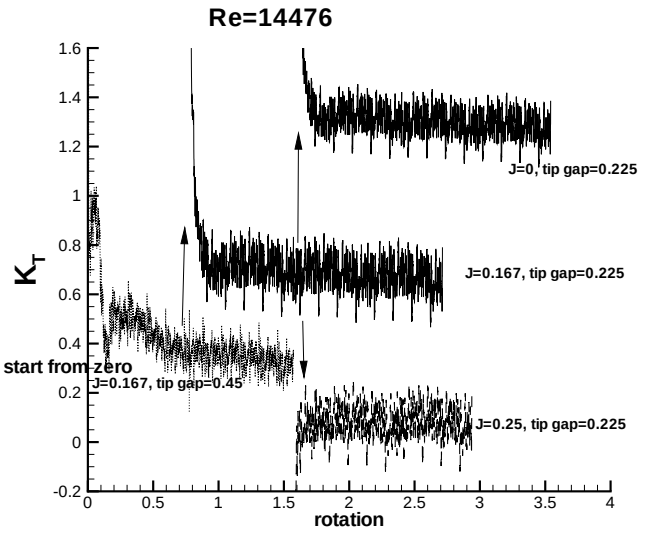

Figure 6. *SPM simulations of waterjet AxWJ-1 at* $Re = 14,476$: Thrust coefficient K_T for different J and tip gap.

Next we examine simulated global quantities and performance of the waterjet. Figure 6 shows the thrust coefficient $K_T = \frac{thrust}{\rho n^2 D^4}$ versus simulation time for different J and tip gap (between the rotor and the casing with inch as its unit) at $Re = 14,476$. The arrows indicate restarting from previous numerical solutions with different parameters. We see that for $J = 0.167$ the thrust increases to almost twice when the tip gap drops to half. The figure also shows that acceleration (increasing J) leads to reduction in K_T whereas deceleration results in larger thrust, which is as expected.

We also present simulation results for the sectional drag coefficient $C_d = \frac{F}{\frac{1}{2}\rho u^2 c \Delta s}$, where Δs is the spanwise length of each section interval of the rotor blade from hub to tip, c is the local chord length and F is the hydrodynamic force for each section interval. Figure 7 shows that C_d drops for increasing advance ratio J at fixed Re or for increasing Re with fixed J. Also, the location of the maximum C_d moves towards the tip of the blade with increasing Re. Furthermore, at $Re = 9050$ the profile and magnitude of C_d is in agreement with the experimental data of the MIT waterjet [16].

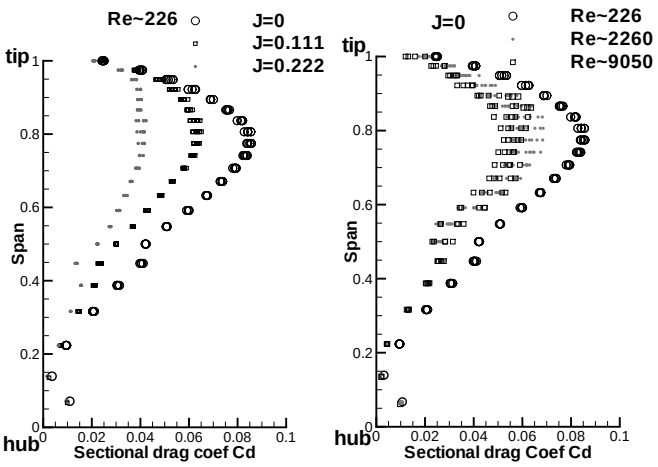

Figure 7. *SPM simulations of waterjet AxWJ-1*: Sectional drag coefficient C_d along the span of rotor blades for different *Re* and *J*.

The robustness and efficiency of our numerical approach enable fast parametric studies for many cases with various advance ratio *J* and Reynolds number *Re*. We calculate the time-averaged thrust coefficient K_T, torque coefficient $K_Q = \frac{torque}{\rho n^2 D^5}$ and efficiency $\eta = \frac{K_T}{K_Q}\frac{J}{2\pi}$. Table 1 lists some typical numerical results compared to the experimental data for an open-water ducted propeller ([17]) with a similar pitch ratio $P/D = 1.0$. We see that similar to the ducted propeller results, the waterjet propulsion system has decreasing thrust and torque with increasing advance ratio at a fixed *Re*. Also, the optimum performance (i.e. maximum efficiency) happens at an intermediate *J* for each *Re*; this optimum *J* increases with increasing *Re*. Furthermore, the table shows that the performance is sensitive to the tip clearance of the rotor, i.e. smaller tip gap leads to larger thrust and also better efficiency. Our numerical results show the right trend towards the design point $Re = 4.4e6, J = 0.486$ with a tip gap of 0.03 inch.

5. SUMMARY AND FUTURE WORK

We have developed and validated an efficient and fast numerical approach for turbulent flows with complex moving domains. It avoids the tyranny of mesh-generation and is a lot faster (typically 1000 times) than ALE codes. The speed-up comes from three facts: (1) simple mesh without conformation to the interfaces and no-remeshing for moving bodies; (2) higher order in temporal and spatial discretization due to the splitting scheme and spectral element method; (3) iterative methods (e.g. conjugate gradient) are faster for simple mesh geometry than deforming and skewed meshes.

We applied this predictive CFD tool to study flows in a waterjet propulsion system (ONR AxWJ-1); important flow features for waterjet design were identified, e.g. flow reversal pockets, which through re-design can be eliminated. We showed that we can capture the laminar-turbulence transition throughout the waterjet system. Also, the hydrodynamic forces on the rotor are shown to be in agreement with experimental data. We have also demonstrated that the combination of simple griding/fast solvers allows extensive parametric study in early-design phase of waterjets, and our preliminary results show good trends towards the operating conditions.

However, the following improvements are recommended for future work. The first objective is validation with experimental data at the exact operating conditions (i.e. larger Re, J and smaller tip clearance). Second, we need to implement more realistic inflow conditions, i.e. non-uniform and fully-turbulent. We can use polynomial chaos analysis [18] to take into account uncertain disturbances in realistic environments. Finally, we need to extend the current methodology to modeling two-phase flows, e.g. to model trapped air at the inlet and also deal with possible cavitation problems.

Table 1. *Waterjet AxWJ-1*: average thrust coefficient K_T and torque coefficient K_Q for various angular velocity ω, Reynolds number *Re*. 'tip gap'=0.225 inch=0.019D.

	Re	*J*	K_T	K_Q	η
open water	10^6	0	0.525	0.044	0
ducted	10^6	0.1	0.47	0.0435	0.172
propeller	10^6	0.6	0.179	0.031	**0.551**
P/D=1.0	10^6	0.83	0	0.017	0
	905	0	1.89	0.241	0
	905	0.083	0.91	0.217	**0.083**
	905	0.125	0.46	0.197	0.046
	905	0.167	0.03	0.179	0.004
	14476	0	1.39	0.167	0
	14476	0.135	0.625	0.129	0.104
	14476	0.167	0.67	0.113	**0.157**
	14476	0.198	0.46	0.104	0.138
	14476	0.250	0.09	0.089	0.040
2∗tip gap	1448	0.167	0.33	0.108	**0.081**
	57906	0	1.24	0.158	0
	57906	0.135	0.81	0.118	0.148
	57906	0.167	0.69	0.110	0.166
	57906	0.198	0.57	0.101	**0.178**
	57906	0.333	0.05	0.075	0.035
$\frac{1}{2}$∗tip gap	57906	0.198	1.08	0.113	**0.301**

6. ACKNOWLEDGEMENTS

This work is supported by the Office of Naval Research N00014-09-1-0160, Sea Basing:T-Craft Dynamic Analysis, and MIT Sea Grant College Program, NA06OAR4170019.

REFERENCES

[1] X. Luo, M. R. Maxey, G. E. Karniadakis, Smoothed profile method for particulate flows: Error analysis and simulations, Journal of Computational Physics 228 (2009) 1750–1769.

[2] Y. Nakayama, K. Kim, R. Yamamoto, Hydrodynamic effects in colloidal dispersions studied by a new efficient direct simulation, in: Flow Dynamics, Vol. 832 of American Institute of Physics Conference Series, 2006, pp. 245–250.

[3] Y. Nakayama, R. Yamamoto, Simulation method to resolve hydrodynamic interactions in colloidal dispersions, Physical Review E 71 (2005) 036707.

[4] R. Yamamoto, K. Kim, Y. Nakayama, Strict simulations of non-equilibrium dynamics of colloids, Colloids and Surfaces A: Physicochemical and Engineering Aspects 311, Issues 1-3 (2007) 42–47.

[5] G. E. Karniadakis, S. J. Sherwin, Spectral/hp Element Methods for CFD, Oxford University Press, New York, 1999.

[6] H. Sun, S. Kinnas, Performance prediction of cavitating water-jet propulsors using a viscous/inviscid interactive method, in: Transactions of the 2008 Annual Meeting of the Society of Naval Architects and Marine Engineers, Houston, Texas, 2008.

[7] S. Schroeder, S.-E. Kim, H. Jasak, Toward predicting performance of an axial flow waterjet including the effects of cavitation and thrust breakdown, in: First International Symposium on Marine Propulsors, 2009.

[8] X. Luo, C. Chryssostomidis, G. E. Karniadakis, Fast 3d flow simulations of a waterjet propulsion system, in: Proc. International Simulation Multi-conference, Istanbul, Turkey, July 2009.

[9] C. S. Peskin, The immersed boundary method, Acta Numerica 11 (2002) 479–517.

[10] G. E. Karniadakis, M. Israeli, S. A. Orszag, High-order splitting methods for the incompressible Navier-Stokes equations, J. Comp. Phys. 97 (1991) 414.

[11] P. R. Spalart, S. R. Allmaras, A one-equation turbulence model for aerodynamic flows, La Recherche Aerospatiale No. 1 (1994) 5–21.

[12] H. Eca, L., A. M., Hay, D. Pelletier, A manufactured solution for a two-dimensional steady wall-bounded incompressible turbulent flow, International Journal of Computational Fluid Dynamics 21 (2007) 175–188.

[13] C. L. Rumsey, Apparent transition behavior of widely-used turbulence models, International Journal of Heat and Fluid Flow 28 (2007) 1460–1471.

[14] J. Boussinesq, Th*é*orie de $l'É$coulement tourbillant, Mem. Pr*é*sent*é*s par Divers Savants Acad. Sci. Inst. Fr. 23 (1877) 46–50.

[15] P. Spalart, C. L. Rumsey, Effective inflow conditions for turbulence models in aerodynamic calculations, AIAA Journal 45 (10) (2007) 2544–2553.

[16] R. W. Kimball, Experimental Investigations and Numerical Modeling of a Mixed Flow Marine Waterjet, PhD. thesis, Dept. of Ocean Engineering, Massachusetts Institue of Technology, June 2001.

[17] J. S. Carlton, Marine propellers and propulsion, London, U.K., Butterworth-Heinemann Ltd., second edition, 2007.

[18] D. Xiu, G. E. Karniadakis, The Wiener-Askey polynomial chaos for stochastic differential equations, SIAM J. Sci. Comput. 24 (2002) 619–644.